(Received 19 May 2026, Accepted 16 June 2026, Scheduled 24 June 2026)

# Analysis and Design of a Dual-Stator Flux Reverse Motor with Irregular Halbach Array

Runqing Su, Zezhou Jin, Qing Long, Jiahao Zhang, and Libing Jing*

*College of Electrical Engineering and New Energy, Hubei Provincial Engineering Technology Research Center for Microgrid, China Three Gorges University, Yichang 443002, China*

**ABSTRACT:** A dual-stator flux reverse motor (DS-FRM) has a simple rotor structure and high output torque. However, a high torque ripple remains a problem. A DS-FRM with an irregular Halbach array is proposed in this study. A small piece of tangentially magnetized permanent magnet (PM) is placed between two radially magnetized PMs. Then, a Multi-Objective Genetic Algorithm (MOGA) combined with the response surface method (RSM) was used to optimize the motor's key parameters. The results show that, compared with the conventional motor, the proposed model achieves a torque increase of 11.51 N·m and a torque ripple reduction of 2.56%. Therefore, this study provides a feasible scheme for the DS-FRM.

## 1. INTRODUCTION

With the rapid development of rail transit and electric vehicles, there is an increasing demand for electric drive systems with high power density and reliability [1]. Permanent magnet synchronous machines (PMSMs) are widely used in these applications because of their high efficiency, compact structure, and excellent dynamic characteristics [2].

According to the location of permanent magnets (PMs), PMSMs can be broadly classified into rotor-PM and stator-PM machines [3]. Stator-PM machines include doubly salient machines [4], flux reversal machines (FRMs) [5], and flux-switching machines [6]. A flux-reversal machine, characterized by a doubly salient structure with PMs mounted on the stator, offers several advantages, such as improved thermal dissipation and reduced requirements for rotor mechanical integrity. Therefore, FRMs have been widely used in traction systems, including metro drives and electric vehicles [7].

In recent years, extensive research on FRMs has been carried out, mainly focusing on the following aspects: Torque enhancement: Researchers have introduced Halbach-array PM configurations into FRMs by placing PMs on both stator and rotor, achieving a significant torque improvement up to 64.2 N·m [8]. In [9], the PMs on the stator teeth were separated and interleaved with iron cores to form consequent poles, effectively reducing flux leakage. In [10], different winding modes, rotor tooth widths, and stator slot width combinations were used to analyze their influence on torque ripple, and various methods to reduce the ripple were summarized. Furthermore, dual-stator configurations have been explored to improve spatial utilization and electromagnetic performance.

To further improve space utilization and electromagnetic performance, a dual-stator flux reverse machine (DS-FRM) has been proposed, in which PMs and armature windings are integrated into two separate stators [11]. This configuration effectively alleviates the geometric conflict between the PMs and armature windings. In [12], the authors proposed a DS-FRM with PMs placed on both the inner stator and rotor, and the results showed that the utilization rate of PMs is increased by 33%. In [13], the application of Halbach-array PMs in DS-FRM was investigated, demonstrating improved air-gap flux density and electromagnetic performance. In addition, Meng et al. proposed two machines that combine consequent poles with a DS-FRM; the first has a better overload capacity, and the second has a higher torque density [14]. Furthermore, in [15], the authors proposed a novel DS-FRM using hybrid excitation, where the output torque was increased by 22.4%, and the back-EMF (Electromotive Force) was also improved.

To further improve the electromagnetic performance, researchers have used many optimization methods. In [16], a multi-objective sensitivity analysis was used to optimize the design of each machine parameter. In [17], the authors used the Response Surface Method (RSM) and Multi-Objective Genetic Algorithm (MOGA) to optimize the machine. In addition, Wang et al. used NSGA2 and RSM to optimize a brushless hybrid excitation motor with a dual-stator configuration [18].

Despite these advancements, DS-FRMs suffer from inherent drawbacks. In particular, the adjacent placement of surface-mounted PMs on the inner stator results in a severe flux leakage. To address this issue, a DS-FRM with an irregular Halbach-array PM configuration is proposed in this study. By using a segmented PM arrangement and introducing tangentially magnetized PMs along the flux path, the proposed design effectively suppressed flux leakage and improved torque performance. The remainder of this study is structured as follows. The topology and operating principle of the proposed motor are introduced in Section 2. The key motor parameters were optimized using RSM and MOGA in Section 3. In Section 4, the

* Corresponding author: Libing Jing (jinglibing163@163.com).

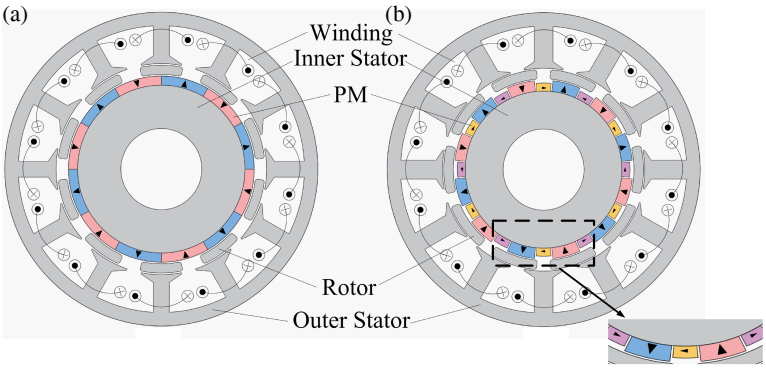


**FIGURE 1**. Topology structure. (a) Conventional and (b) proposed.

electromagnetic performance of the proposed motor is analyzed and discussed. Finally, a summary of the article is presented in Section 5.

## 2. TOPOLOGY AND OPERATION PRINCIPLE

### 2.1. Topology

Figure 1 shows two different DS-FRM structures. Both motors employ a 10-pole/12-slot configuration and share the same main structural parameters to ensure a fair and effective comparison. Fig. 1(a) shows the conventional DS-FRM, in which the PMs are continuously arranged. The primary difference between the two motors lies in the arrangement of the inner stator permanent magnets.

As shown in Fig. 1(b), the design separates the originally continuous PMs into discrete pieces. To guide and enhance the magnetic flux distribution, tangential PMs are arranged along the magnetic flux path and inserted between adjacent radial PMs. On the inner stator, these PMs were placed sequentially in four directions radially inward, tangentially right, radially outward, and tangentially left, forming a Halbach array. Notably, the tangential PMs differed from the radial PMs in terms of both length and width. The structure forms an irregular Halbach array.

Table 1 presents the key design parameters of the motor.

**TABLE 1**. Motor parameters.

| Parameters | Values |
|---|---|
| Rated speed (r/min) | 600 |
| Air gap (mm) | 0.5 |
| Outer radius of Outer Stator (mm) | 58 |
| Outer radius of Rotor (mm) | 37 |
| Stator tooth width (deg) | 4.5 |
| Rotor tooth width (deg) | 14 |
| Stack length (mm) | 55 |
| Rated current (A) | 10 |

### 2.2. Operation Principle

The working principle of the DS-FRM with an irregular Halbach array is also based on the principle of magnetic field modulation. The motor has two irregular air gaps, and there are also two air-gap flux density distributions. One of them is the flux density modulated by the rotor by the magnetomotive force (MMF) generated by the inner stator PM, and the other is the flux density modulated by the rotor after the MMF generated by the armature winding is introduced into the three-phase alternating current. Since this study focuses on the air-gap flux density under zero-current conditions, only the PM-excited magnetic field in the inner air-gap is analytically investigated.

Figure 2 shows a simplified MMF motor of a no-load PM. Given that only the radial air-gap flux density is calculated, the two tangentially magnetized PMs are neglected in the analytical model. At this time, the MMF generated by the PM can be expressed as,

$$\begin{cases} F(\theta) = \sum_{n=1}^{\infty} F_{PMn} \sin(mP_{PM}\theta) \\ F_{PMn} = -\dfrac{2F_{PM}}{m\pi} \cos(mP_{PM}\theta_1) \end{cases} \tag{1}$$

where $m$ is a constant, $F_{PMn}$ the harmonic MMF amplitude, $P_{PM}$ the polar logarithm of PM, and $\theta_3$ the spatial mechanical angle.

The simplified permeance model generated by the salient pole of the rotor is shown in Fig. 3. The simplified permeance can be expressed as,

$$\begin{cases} \Lambda(\theta) = \Lambda_0 + \sum_{k=1}^{\infty} \Lambda_k \cos(nN_r\theta - \omega_r t) \\ \Lambda_0 = \dfrac{N_r}{\pi}\Lambda_1\theta_3 \\ \Lambda_k = \dfrac{2\Lambda_1}{\pi n} \sin(nN_r\theta) \end{cases} \tag{2}$$

where $n$ is a constant, $\omega_r$ the rotation speed of the rotor, $N_r$ the pole-pair number of the rotor, and $\Lambda_0$ the amplitude of the wave of the permeance.

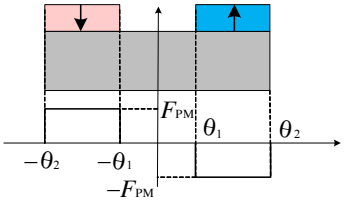


**FIGURE 2**. Simplified magnetomotive force model of inner-stator PMs.

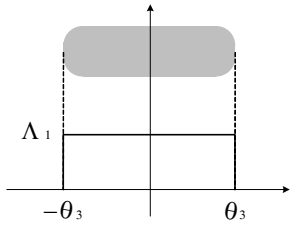


**FIGURE 3**. Simplified diagram of rotor salient pole permeance model.

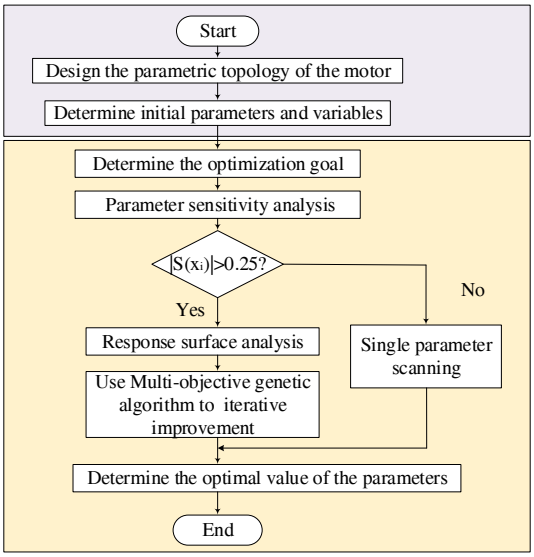


**FIGURE 4**. Multi-objective optimization flowchart.

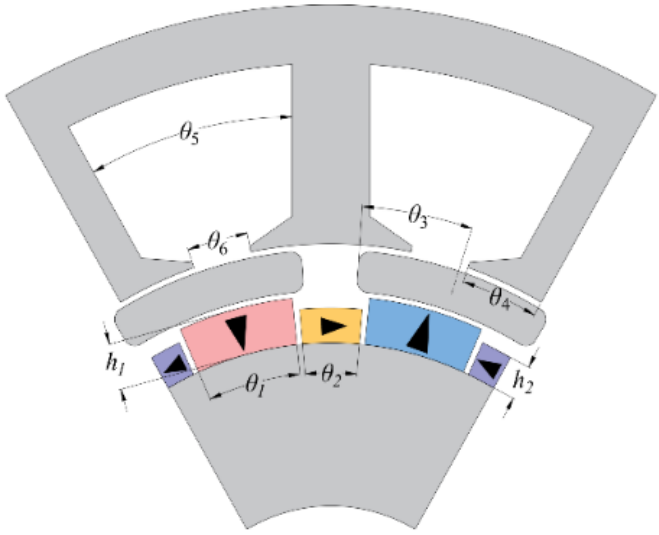


**FIGURE 5**. Local structure diagram of motor and geometric parameters labeling.

Therefore, the excitation magnetic flux density produced by the PMs of the inner stator together with the rotor can be expressed as,

$$\begin{aligned} B_r =& F(\theta)\cdot\Lambda(\theta) = \Lambda_0 \sum_{n=1}^{\infty} F_{PMn}\sin(mP_{PM}\theta) \\ &+ \sum_{n=1}^{\infty}\sum_{k=1}^{\infty}\frac{F_{PMn}\Lambda_k}{2}\left[\sin\left(\left(mP_{PM}+nN_r\right)\theta-\omega_r t\right)\right. \\ &\left.+\sin\left(\left(mP_{PM}-nN_r\right)\theta+\omega_r t\right)\right] \end{aligned} \tag{3}$$

According to Eq. (3), Table 2 shows the expressions for the working harmonics of this motor. According to the modulation relationship in Table 2, the 6th harmonic corresponds to the minimum modulation coefficient ($m = 1, n = 0$) and therefore exhibits the highest amplitude, making it the dominant working harmonic.

**TABLE 2**. Working harmonic expression of modulated.

| Harmonic Order | Rotational Speed |
|---|---|
| $\lvert mP_{PM}\rvert$ | 0 |
| $\lvert mP_{PM}\pm nN_r\rvert$ | $nN_r\omega_r/(mP_{PM}\pm nN_r)$ |

## 3. MULTI-OBJECTIVE OPTIMIZATION

To further improve the comprehensive electromagnetic performance of the proposed motor, a multi-objective optimization design for key structural parameters was performed. The optimization process was conducted by considering torque and torque ripple simultaneously, with the objectives of maximizing the average torque while minimizing the torque ripple.

The overall process of multi-objective optimization is shown in Fig. 4, which includes the following stages: design machine stage and optimization calculation stage.

### 3.1. Parameter Optimization Analysis

To improve optimization efficiency, a sensitivity analysis was first performed to evaluate the impact of each parameter on motor performance and identify high-sensitivity ones, as shown in Fig. 5. The sensitivity index was calculated using:

$$|S(x_i)| = \lambda_1\left|G_{(oi)}(x_i)\right| + \lambda_2\left|G_{(kri)}(x_i)\right| \tag{4}$$

where $G_{(oi)}(x_i)$ and $G_{(kri)}(x_i)$ are the torque and torque ripple under the design variables, and $\lambda_1 = \lambda_2 = 0.5$ are the weight coefficients. Based on the calculated sensitivity indices, parameters with $|S(x_i)| > 0.25$ were defined as highly sensitive, whereas those with $|S(x_i)| < 0.25$ were defined as lowly sensitive. Therefore, the PM length, rotor tooth width, and stator tooth yoke width were selected for the subsequent RSM optimization. MOGA was then employed to perform a global opti-

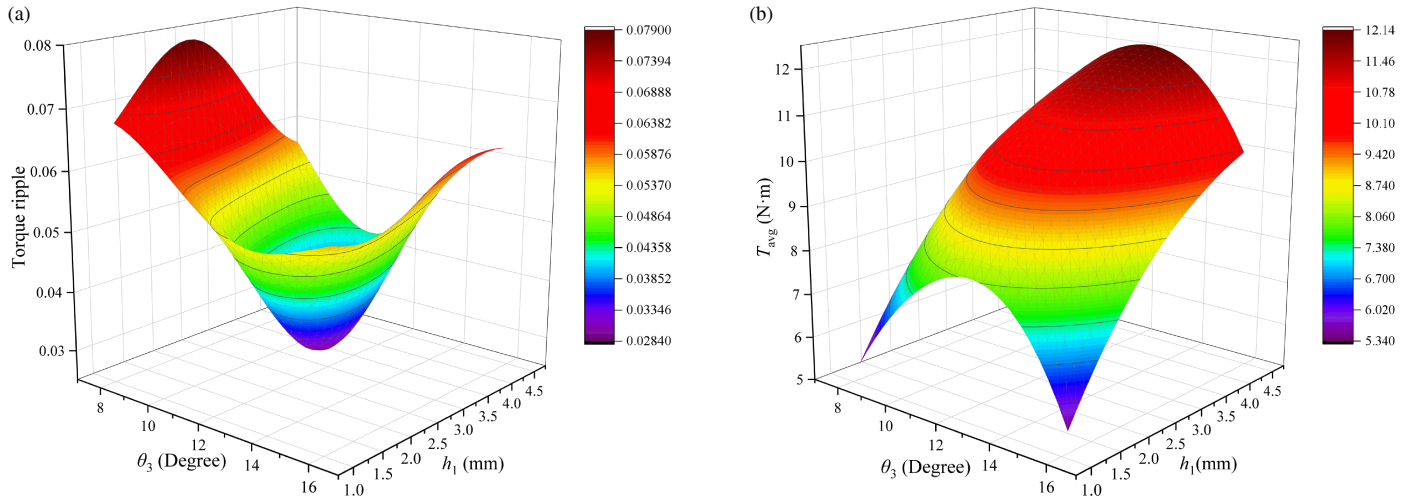


**FIGURE 6**. Response surface of $\theta_3$ and $h_1$. (a) Torque ripple and (b) torque.

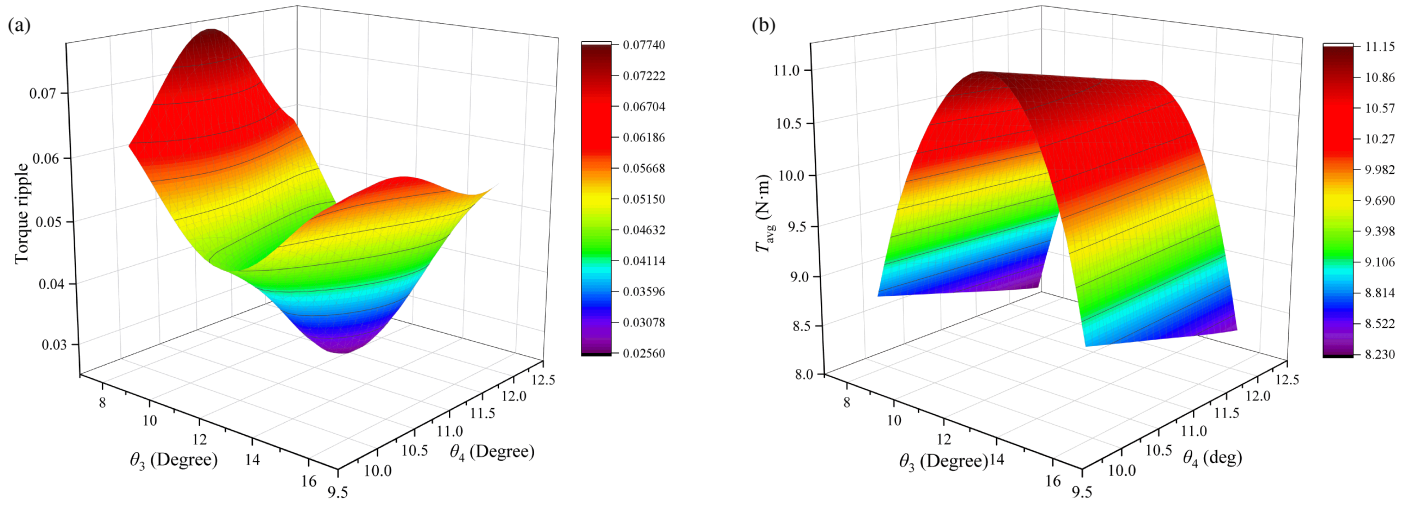


**FIGURE 7**. Response surface of $\theta_3$ and $\theta_4$. (a) Torque ripple and (b) torque.

mization search on these high-sensitivity parameters to obtain an optimal parameter combination.

The range of parameter optimization is shown in Table 3, and the MOGA is employed to maximize torque and minimize torque ripple.

**TABLE 3**. Optimization range of key parameters.

| Parameters | Optimal range |
|---|---|
| Height of PM $h_1$/mm | 3–5 |
| Width of rotor $\theta_3$/deg | 12–16 |
| Width of stator yoke $\theta_4$/deg | 9.5–13 |

Figure 6 shows the influence of the rotor tooth width and PM height on the torque and torque ripple of the motor. It can be seen from the figure that when $\theta_3 = 12°$ and $h_1 = 3.5$ mm, the torque ripple reaches the minimum value, and the torque also reaches the maximum value at $\theta_3 = 12°$, but the corresponding $h_1$ is 4.3 mm. It is worth noting that when $h_1 < 4$ mm, the torque growth is more significant; when $h_1 > 4$ mm, the amount of PM increases sharply, but the torque increase tends to be gentle.

The influence of the rotor and stator tooth widths on the torque and torque ripple of the motor is illustrated in Fig. 7. As observed from the figure, the minimum torque ripple is obtained when $\theta_3 = 12.5°$ and $\theta_4 = 11.47°$. Meanwhile, the torque increases with the decrease in $\theta_4$, and the maximum value is obtained at $\theta_3 = 12.5°$ and $\theta_4 = 9.9°$.

The influence of stator tooth width and PM thickness on the torque and torque ripple of the motor is shown in Fig. 8. When $\theta_4 = 11.44°$ and $h_1 = 2.5$ mm, the torque ripple reaches the minimum value; the torque increases with the increase in torque; and the maximum value is obtained at $\theta_4 = 9.9°$ and $h_1 = 4.3$ mm.

Figure 9 shows the distribution of the candidate points obtained using MOGA. As the average torque increases, the torque ripple tends to increase simultaneously, indicating an inherent trade-off between torque output and torque ripple performance. Since the primary objective of this study is to minimize torque ripple, torque ripple is selected as the key opti-

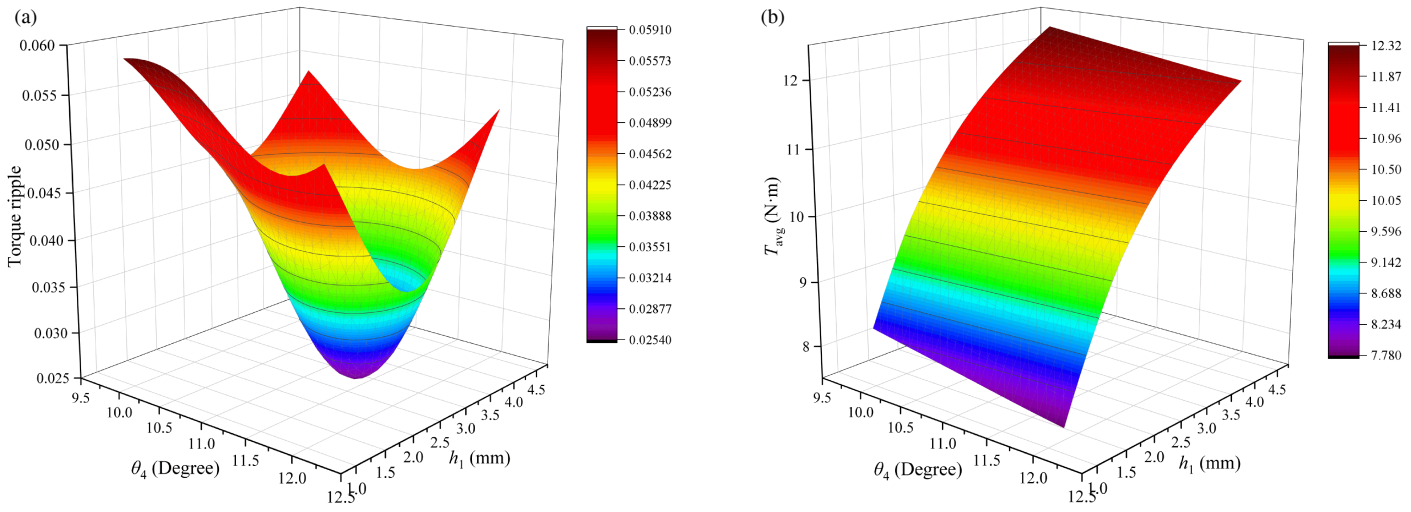


**FIGURE 8**. Response surface of $\theta_4$ and $h_1$. (a) Torque ripple and (b) torque.

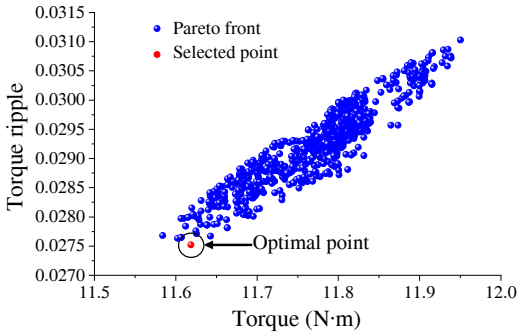


**FIGURE 9**. Optimization result graph based on MOGA.

mization criterion for evaluating the Pareto-optimal solutions. Therefore, the red-marked candidate point is selected because it achieves the maximum torque while maintaining a relatively low torque ripple. In this way, a desirable balance between torque enhancement and torque ripple suppression is achieved. Subsequently, the final optimal design is determined through a single-parameter scanning process.

As shown in Table 4, the optimal values of the high-sensitivity parameters were obtained based on the RSM.

**TABLE 4**. The optimal value of the key parameters.

| Parameters | Final value |
|---|---|
| Height of PM $h_1$/mm | 4 |
| Width of rotor $\theta_3$/deg | 12.5 |
| Width of stator yoke $\theta_4$/deg | 9.9 |

## 4. ELECTROMAGNETIC PERFORMANCE

To evaluate the capability of the proposed model, a comprehensive comparison of the electromagnetic performance was conducted. Both the conventional DS-FRM and the proposed motor were optimized using the same RSM/MOGA to ensure a fair comparison. Based on Finite Element Analysis (FEA), the field distributions, back-EMF, and torque of the motor were calculated and analyzed.

### 4.1. Flux Distributions

Figure 10 shows the flux and magnetic flux density distributions. As shown in the figure, the proposed irregular Halbach array motor effectively reduces the flux leakage phenomenon at the PM connection, whereas the conventional motor suffers from severe flux leakage in this region. Therefore, the torque of the proposed motor was significantly improved.

Figure 11 shows the waveform of the radial air-gap flux density and the harmonic spectrum after the Fourier decomposition. As discussed previously, the 6th harmonic is the dominant working harmonic, and as shown in the figure, the proposed motor exhibits a slightly higher working harmonic amplitude while effectively suppressing other non-working harmonics, such as the 18th, 30th, and 42nd orders. Therefore, these harmonic changes contribute to the improvement of torque.

### 4.2. Phase Back-EMF

The back-EMF is an important indicator of the air-gap magnetic field distribution and directly affects the torque production capability and the motor's dynamic performance.

Figure 12 shows the waveform of the back-EMF and its Fourier harmonic spectrum. The back-EMF amplitude of the proposed motor is slightly increased from 36.19 V to 37.02 V. More importantly, the fundamental component is enhanced, while the harmonic components are effectively suppressed after optimization. As a result, the total harmonic distortion (THD) is reduced from 1.49% to 0.68%, indicating a significant improvement in the sinusoidal quality of the back-EMF waveform.

### 4.3. Torque

Torque performance analysis is the key to motor performance analysis, which mainly includes a comparative analysis of cogging torque, average electromagnetic torque, and torque ripple.

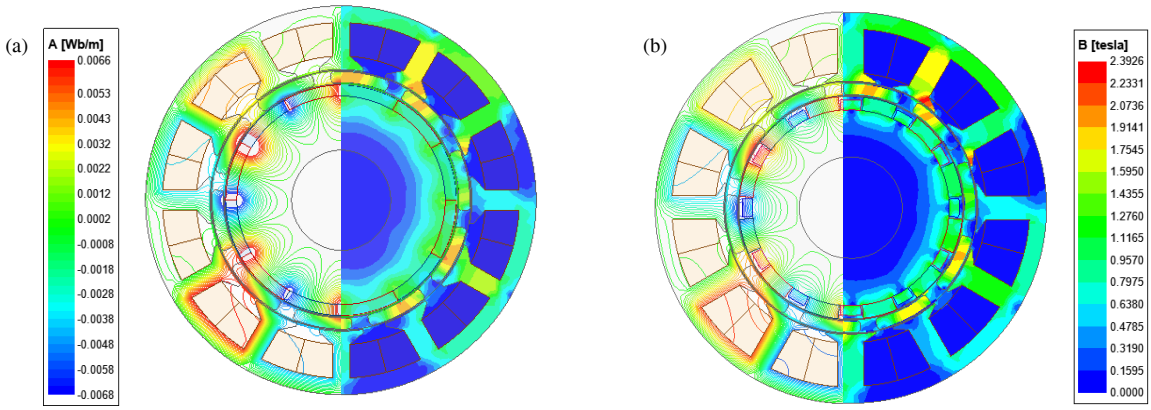


**FIGURE 10**. Flux distributions. (a) Conventional and (b) proposed.

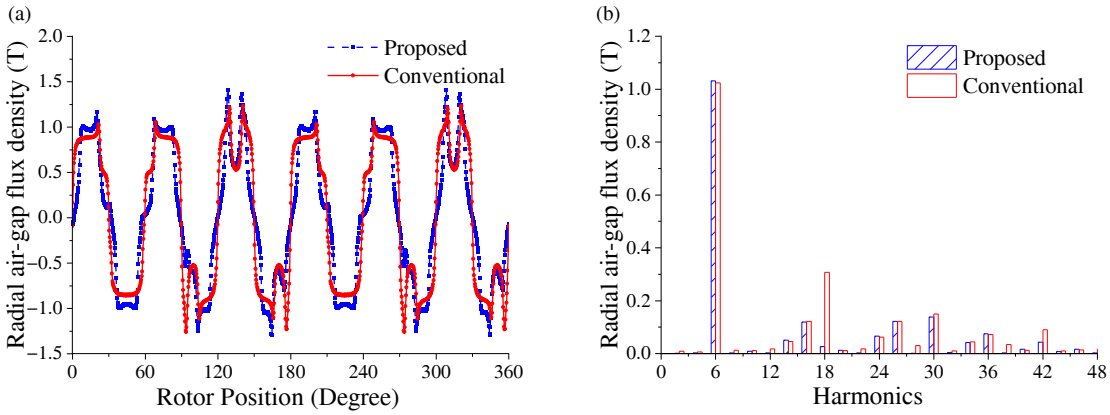


**FIGURE 11**. Flux density. (a) Waveform and (b) harmonic spectrum.

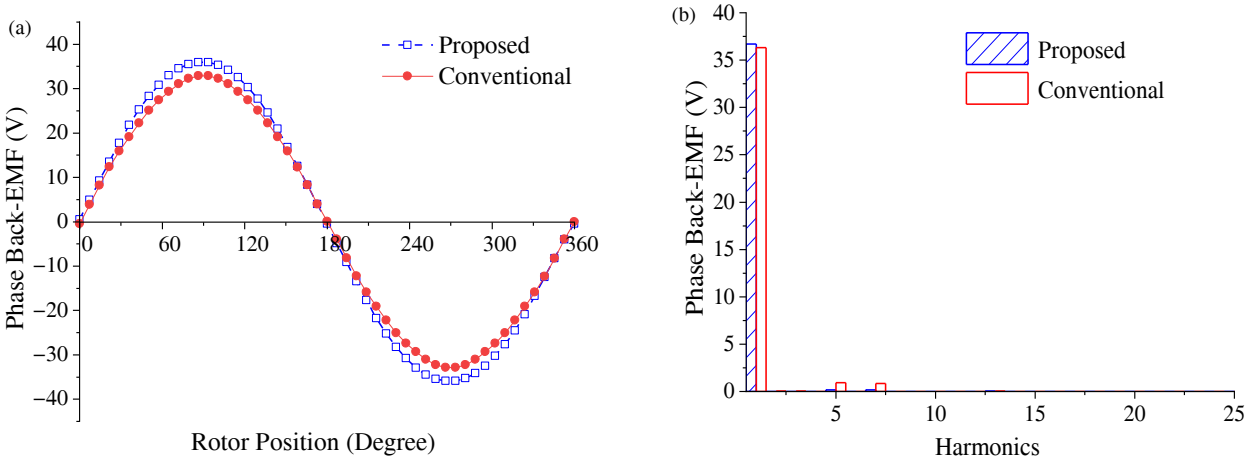


**FIGURE 12**. Back-EMF. (a) Waveform and (b) harmonic spectrum.

The torque ripple is calculated as,

$$T_{ri} = \frac{T_{\max} - T_{\min}}{T_{avg}} \times 100\% \tag{5}$$

where $T_{max}$, $T_{\min}$, and $T_{avg}$ are the maximum, minimum, and average torques, respectively.

Figure 13 shows that the cogging torque of the proposed motor is significantly lower than that of the conventional motor. The amplitude was reduced from 105 mN·m to 7.6 mN·m. The proposed motor is responsible for this decrease because it effectively suppresses variations in the magnetic reluctance across the air gap.

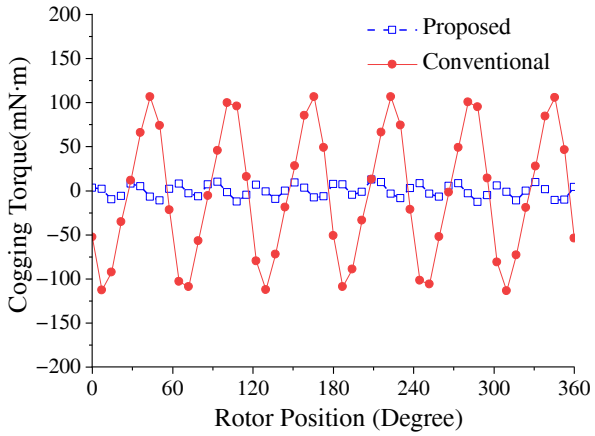


**FIGURE 13**. Cogging torque.

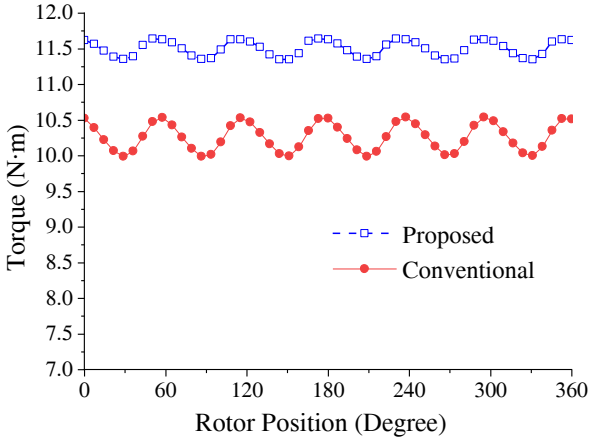


**FIGURE 14**. Output torque.

**TABLE 5**. Comparison of output torque in all aspects.

| Type | $T_{min}$/(N·m) | $T_{max}$/(N·m) | $T_{avg}$/(N·m) | $T_{ri}$/(%) |
|---|---|---|---|---|
| I | 9.99 | 10.54 | 10.26 | 5.39 |
| II | 11.35 | 11.64 | 11.51 | 2.56 |

Note: I-Conventional motor, II-Proposed motor

**TABLE 6**. Performance comparison.

| Parameters | Conventional | Proposed |
|---|---|---|
| PMs volume ($cm^3$) | 37.3494 | 36.2538 |
| Torque (N·m) | 10.26 | 11.51 |
| Torque density ($kN·m/m^3$) | 17.65 | 19.80 |
| T/PMV ($kN·m/m^3$) | 274.7 | 317.5 |

Figure 14 shows that the torque of the conventional motor is 10.26 N·m, and the output torque of the proposed motor is 11.51 N·m, which is an increase of 12.18%. The torque ripple of the conventional motor is 5.39%, whereas that of the proposed motor was 2.56%, which is a reduction of 52.5%.

Table 5 shows the minimum, maximum, and average values of the output torque as well as the torque ripple of the proposed motor.

Table 6 shows a comparison of the performance of the two motors. The torque density of the proposed motor is 19.80 $kN·m/m^3$, which is 12.18% higher than that of the conventional motor. The ratio of the torque of the improved motor to the volume of the PM was 317.5 $kN·m/m^3$, which was increased by 15.58%.

## 5. CONCLUSION

In this study, a DS-FRM with an irregular Halbach array is discussed, aiming to reduce magnetic flux leakage by optimizing the magnetic field distribution, thereby decreasing the torque ripple. Based on the FEA, the proposed motor demonstrated the following advantages compared with a conventional motor;

1) The 6th harmonic maintained the main working harmonic advantage, and other non-working harmonics were effectively suppressed. The amplitude of the back-EMF increased from 36.19 to 37.02 V, effectively improving the sinusoidal degree of the waveform.

2) The cogging torque amplitude was significantly reduced from 105 mN·m to 76 mN·m. The output torque was increased to 11.50 N·m, representing an improvement of 12.18%, and the torque ripple was further decreased from 5.39% to 2.56%.

## ACKNOWLEDGEMENT

This work was supported by the National Natural Science Foundation of China (grant No. 52477056).

## REFERENCES

[1] Zhu, Z. Q. and D. Howe, "Electrical machines and drives for electric, hybrid, and fuel cell vehicles," *Proceedings of the IEEE*, Vol. 95, No. 4, 746–765, 2007.

[2] El-Refaie, A. M., "Motors/generators for traction/propulsion applications: A review," *IEEE Vehicular Technology Magazine*, Vol. 8, No. 1, 90–99, 2013.

[3] Zhu, X., C. H. T. Lee, C. C. Chan, L. Xu, and W. Zhao, "Overview of flux-modulation machines based on flux-modulation principle: Topology, theory, and development prospects," *IEEE Transactions on Transportation Electrification*, Vol. 6, No. 2, 612–624, 2020.

[4] Yi, L. and M. Zhao, "Doubly salient permanent magnet motor development review," in *2013 Third International Conference on Instrumentation, Measurement, Computer, Communication and Control*, 1513–1516, Shenyang, China, 2013.

[5] More, D. S. and B. G. Fernandes, "Analysis of flux-reversal machine based on fictitious electrical gear," *IEEE Transactions on Energy Conversion*, Vol. 25, No. 4, 940–947, 2010.

[6] Lee, C. H. T., J. L. Kirtley, and M. Angle, "A partitioned-stator flux-switching permanent-magnet machine with mechanical flux adjusters for hybrid electric vehicles," *IEEE Transactions on Magnetics*, Vol. 53, No. 11, 1–7, 2017.

[7] Wu, W., S. Niu, M. Jiang, and Y. Wang, "Design and optimization of a novel flux reversal permanent magnet machine with DC excitation source," in *2023 26th International Conference on Electrical Machines and Systems (ICEMS)*, 2765–2769, Zhuhai, China, 2023.

[8] Aslani, B., S. E. Abdollahi, and S. A. Gholamian, "A novel dual-PM flux reversal machine with Halbach array magnets in stator slots," in *2023 3rd International Conference on Electrical Machines and Drives (ICEMD)*, 1–5, Tehran, Iran, 2023.

[9] Bai, X., X. Yang, Y. Meng, and S. Fang, "A new consequent pole flux-reversal permanent magnet machine with auxiliary teeth," in *2023 IEEE International Conference on Applied Superconductivity and Electromagnetic Devices (ASEMD)*, 1–2, Tianjin, China, 2023.

[10] Suriano-Sánchez, S. I., M. Ponce-Silva, V. H. Olivares-Peregrino, and S. E. D. León-Aldaco, "A review of torque ripple reduction design methods for radial flux PM motors," *Eng*, Vol. 3, No. 4, 646–661, 2022.

[11] Aslani, B., S. E. Abdollahi, and S. A. Gholamian, "A novel dual-PM flux reversal machine with Halbach array magnets in stator slots," in *2023 3rd International Conference on Electrical Machines and Drives (ICEMD)*, 1–5, Tehran, Iran, 2023.

[12] Meng, Y., S. Fang, Y. Li, Y. Zhong, and L. Qin, "Design and analysis of new dual-stator flux modulated machines with dual-PM excitation," *IEEE Transactions on Industry Applications*, Vol. 59, No. 2, 1383–1393, 2023.

[13] Aslani, B., S. A. Gholamian, and S. E. Abdollahi, "Analysis of a double stator flux reversal permanent magnet machine with halbach array magnets," in *2023 14th Power Electronics, Drive Systems, and Technologies Conference (PEDSTC)*, 1–6, Babol, Iran, 2023.

[14] Meng, Y., S. Fang, Y. Zhu, Y. Yu, and L. Qin, "Investigation of new dual-stator consequent-pole flux reversal permanent magnet arc machines," *IEEE Transactions on Applied Superconductivity*, Vol. 34, No. 8, 1–5, 2024.

[15] Ning, S., P. Seangwong, N. Fernando, J. Jongudomkarn, A. Siritaratiwat, and P. Khunkitti, "A novel double stator hybrid-excited flux reversal permanent magnet machine with halbach arrays for electric vehicle traction applications," *IEEE Access*, Vol. 11, 113 255–113 263, 2023.

[16] Zhang, S., W. Zhang, R. Wang, X. Zhang, and X. Zhang, "Optimization design of halbach permanent magnet motor based on multi-objective sensitivity," *CES Transactions on Electrical Machines and Systems*, Vol. 4, No. 1, 20–26, 2020.

[17] Zhang, B., M. Cheng, R. Cao, Y. Du, and G. Zhang, "Analysis of linear flux-switching permanent magnet motor using response surface methodology," *IEEE Transactions on Magnetics*, Vol. 50, No. 11, 1–4, 2014.

[18] Wang, X., Y. Fan, X. Lu, Q. Chen, and C. H. T. Lee, "Multiobjective optimization of a dual stator brushless hybrid excitation motor based on response surface model and NSGA 2," *IEEE Transactions on Industry Applications*, Vol. 58, No. 5, 6105–6114, 2022.